Growth and dispersion of the Shoemaker-Levy 9 impact features from HST imaging

By RETA F. BEEBE

Department of Astronomy, New Mexico State University, P.O. Box 30001/Dept. 4500, Las Cruces, NM 88003, USA

The Hubble Space Telescope Wide Field Planetary Camera 2 imaging data provide the highest spatial resolution of individual Shoemaker-Levy 9 impact sites. Analysis of images obtained with the F410M filter yielded horizontal translation rates of tropospheric cloud structures and the east-west components have been interpreted as zonal winds which vary with latitude. When the tropospheric zonal winds between $-60°$ and $-30°$, which were derived from the SL9 images, are compared with Voyager data there are no discernible changes in the magnitude or latitudinal positions of wind minima and maxima. This result provides additional evidence of the long-term stability of the zonal winds. Changes in individual sites during a two week period in July 1994 have been mapped. Their evolution is consistent with zonal winds decreasing with height and it provides evidence that local circulation associated with isolated weather systems perturbs the lower stratosphere.

1. Introduction

On July 16, 1994 at 21^h30–51^m the first multicolor images revealed the site of the A fragment impact of Comet P/Shoemaker-Levy 9 (SL9) as it rotated into view about 1.5 hours after it formed. The lack of color dependence and the resulting orientation and morphology of the ejecta blanket had not been anticipated. The blowout region was located more to the east than expected and dark rings and crescent-shaped structures centered on the impact site were observed, but the most obvious aspect of site A was the dark core (see the chapter by Hammel). Due to the fact that the dark debris were in the stratosphere, the extent and contrast of the extended ejecta were strongly enhanced near the limb and terminator. This aspect of the SL9 sites is unique in the history of visual observations of Jupiter (Reese, 1994).

This study utilizes HST/WFPC2 SL9 Campaign imaging data to derive tropospheric winds from $-60°$ to $-30°$ latitude and compares them to Voyager results obtained from data with the same spatial resolution (unless otherwise specified all latitudes are planetographic and all longitudes are in System III—see section 2 for definitions). The temporal changes of the impact sites are interpreted relative to this underlying tropospheric wind field. The effects of local cyclonic and anticyclonic storm systems are considered in an effort to determine the extent to which the tropospheric wind field and the vertical propagation of organized storm systems influence stratospheric circulation.

Temporal variability of the reflectivity and longitudinal drift rates of large, long-lived cloud systems had been well documented long before the SL9 fragments impacted Jupiter (Peek, 1958; Smith & Hunt, 1976; Beebe & Youngblood, 1979; Smith, *et al.* 1979a & 1979b; Beebe, Orton & West, 1989). Quantification of variations of the magnitude of the zonal winds and latitudinal positions of the jets (maxima and minima of the east-west component of the tropospheric winds) was hampered by the fact that coherent cloud systems, which can be resolved in groundbased observations, tend to interact with the local wind field, rotate about their centers and translate eastward or westward at a rate equivalent to the zonal wind at the central latitude. Consequently, historical zonal wind

https://doi.org/10.1017/S0252921100115568 Published online by Cambridge University Press

profiles (east-west wind component versus latitude) (Peek, 1958; Chapman, 1969; Smith & Hunt, 1976; Beebe & Youngblood, 1979) had lower wind speeds associated with the zonal wind maxima and minima than those obtained from analysis of the more highly resolved Voyager imaging data where cloud markers that drifted with the winds could be resolved (Ingersoll, *et al.* 1981; Limaye, *et al.* 1982; Limaye, 1986; Beebe, Orton & West, 1989).

Because there is no terrestrial equivalent to the strong westerly (west-to-east) winds that dominate cloud structure at low Jovian latitudes, considerable effort has been expended to understand global circulation (Ingersoll & Cuzzi, 1969; Williams & Wilson, 1988; Dowling & Ingersoll, 1989; Stone, 1976; Dowling, 1993; Marcus, 1993). Much of the temporal information concerning long term stability of winds has been derived from images spanning the visible range (0.4 to 0.7 micron) of the spectrum. Broadband transmission filters, which sound down to the ammonia cloud deck (0.5 to 0.7 bars) have generally been used to record temporal changes in the cloud deck. Because these filters do not vertically sample the atmosphere, our knowledge of variation of winds with altitude within Jupiter's atmosphere is limited. The rate of decrease of zonal winds with altitude above the visible cloud deck has been derived from interpretation of the Voyager infrared spectroscopic data (Gierasch, Conrath & Magalhaes, 1986). In addition, stratospheric and upper tropospheric circulation has been modeled by West, Friedson & Appleby (1992). Although it is understood that the magnitude of zonal winds must go to zero relative to the rate of rotation of the bulk of the planet, there are few observational constraints which define the depth to which zonal winds penetrate. Ingersoll, Beebe, Conrath & Hunt (1984) have argued in favor of deep penetration of the winds in order to explain Saturnian winds, which, at the level of the visible cloud deck, blow from west to east over most of the planet.

Throughout the Voyager era, detectors capable of high spatial resolution were limited to visible wavelengths. A review by West, Strobel & Tomasko (1986) summarizes the extent to which these data constrained models of the upper atmosphere. Development of infrared sensitive detectors and narrow-band interference filters has allowed the strong frequency dependence of the methane gas to be utilized to selectively sound the atmosphere above the ammonia cloud deck (Orton, *et al.* 1994). Low IR emissivity tends to correlate with low reflectivity of clouds at visible wavelengths; however, infrared monitoring reveals nonseasonal variability and a lack of correlation between IR emission and low cloud reflectivity within cyclonic regions, such as the South Equatorial Belt and North Temperate Belt, which display aperiodic convective disturbances.

Gierasch & Conrath (1993) point out that, until probes have measured conditions below the ammonia cloud deck at a sufficient number of latitudes, the atmospheric energy balance will not be well understood. Although Mac Low and Zahnle (see their chapters) claim that comet fragments may have penetrated no further than 200 millibars, hopefully the December 7, 1995 entry of the Galileo probe is the first of a series of future probes to sound down through the water cloud at various latitudes. In the meantime, the Hubble Space Telescope (HST) Wide Field Planetary Camera 2 (WFPC2), Faint Object Camera, Faint Object Spectrograph and Goddard High Resolution Spectrograph provide ultraviolet capabilities and spatial resolution more than ten times better than can be obtained from Earth. These instruments allow sensing of the upper atmosphere over a wavelength range from 0.12 to 1.0 microns. Unlike the Voyager high resolution data, which spanned a few months, HST (with high resolution cameras and spectroscopic instruments) has a nominal expectancy of about 15 years, more than a Jovian year.

The WFPC2 allows two modes of operation; planetary camera mode (PC) samples at 0.0455 arcsec/pixel and wide field mode (WF), using detector 3, samples at 0.0995

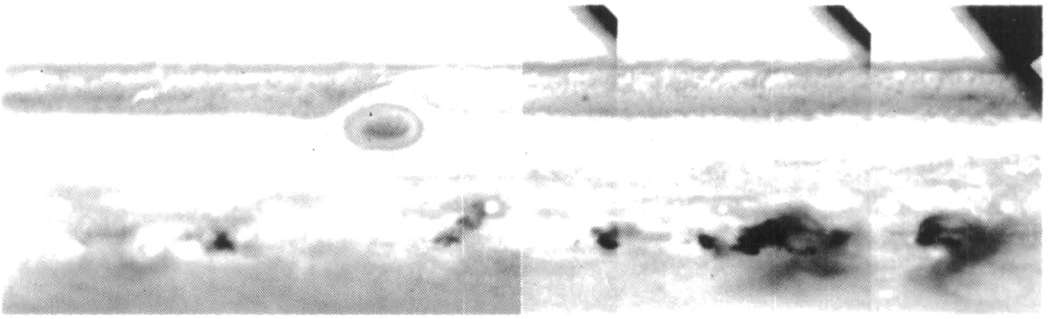

FIGURE 1. Latitude-Longitude map of impact sites. This map extends from −65° to 5° in latitude and (left to right) from 205° through 0° to −35°(325°) W longitude. These data were obtained on July 23, 1994. The A, E, H, Q1, R, G-S and L sites are visible from left to right in the projection.

arcsec/pixel (Burrows, *et al.* 1994; Holtzman, *et al.* 1995). For the SL9 data, this leads to a pixelation scale at the sub-spacecraft point on Jupiter of 170 and 375 km, respectively (although the resolution of the PC mode of WFPC2 is somewhat poorer than the pixelation scale, Wiener deconvolution of F410M images with a theoretical point-spread function increased the contrast but neither positively enhanced the resolution nor negatively introduced systematic structure in the data). Figure 1 illustrates the effective resolution of these two modes of operation. This latitude-longitude map is composed of WF images (left) and PC (right) images projected to optimize the PC resolution. The images were enhanced by removing large scale limb-darkening with a Minnaert filter (Minnaert, 1941) where

$$B(\mu, \mu_0) = B_0(\mu, \mu_0)^k/\mu, \qquad 0.0 < k < 1.0 \tag{1.1}$$

is the estimated surface brightness expressed as a function of the cosine of the local emergent, μ, and incident, μ_0, angles and B_0 is the value when μ and μ_0 equal 0. The value of k can be determined by a least squares fit of the log of equation 1.1 and although this function has no physical significance, it is an effective scene flattener. The brighter the limb of the planet, the smaller the k value will be; for example, $k = 0.5$, 0.6 and 1.0 are effective for the F336W, F410M and 890-nm methane filters, respectively. After the large scale limb darkening was removed, the contrast of the remaining high frequency component of the images was enhanced and maps like the one shown in Figure 1 were constructed. In regions where images obtained in consecutive HST orbits overlap, selection of the brightness value from the image with maximum value of $(\mu \times \mu_0)$ yields the most consistent longitudinal contrast. In the case of a remote planet like Jupiter, the incident sunlight and emergent viewing angle are similar, therefore this criterion selects regions closest to the central meridian or samples the underlying clouds through minimum path lengths of the overlying hazes and Rayleigh scatterers.

The following analysis and discussion is based on imaging data, obtained by the HST/SL9 Campaign. Two major constraints limit interpretation of the evolution of individual impact sites. Because there is considerable vignetting in the methane filter, the WF mode was frequently used to obtain photometrically calibrated global coverage. In addition, the telescope was shared with other non-SL9 programs during the week of impacts, resulting in less than optimal (10-hr. intervals) sampling. Observing constraints were such that there was 38 to 42 min. of observing time during each 96 min. orbit. WFPC2 is an all purpose camera, optimized for imaging faint objects, therefore it does not have a fast readout option. Nominal setup and readout time is about 3 minutes per

Image ID	Time d/hr/min	Mode	CM(sys III)†	Elapsed Time (hr)	Elapsed Rotations
u2fi0h05	17/17/09	WF	120.33	0.00	0.00
u2fi0w05	19/09/20	PC	137.67	40.18	4.05
u2fi1c05	21/09/35	PC	87.54	88.43	8.91
u2fi1m05	22/06/34	WF	128.54	109.41	11.02

† System III latitude is defined as L(t) = 217.956 + 870.536 deg/day(t-t_0), where t_0 = 0 hr UT Jan 1, 1965 in Riddle, A. C. & Warwick, J. W. 1976 Redefinition of System III Longitude, *Icarus* **27**, 457–459.

TABLE 1. July 1994 images used to measure the zonal winds

exposure; and, depending on the filters and whether new guide stars had to be acquired, 9–13 images were obtained within a given orbit. Although images with filters F953N, FQCH4N15 (889 nm), F673N, F555W (PC), F547M (WF), F410M, F336W, F255W, F218W are available (where W, M and N indicate wide, medium and narrow bandpasses and the three digits the effective wavelength of the filter in nm), in this analysis the 410, 889, 336, and 255-nm images have been utilized to define the extent of the impact sites and the 410-nm images to measure horizontal wind fields.

2. Zonal winds

A set of images obtained with the F410M filter was selected to measure the zonal (east-west) tropospheric winds. This filter is similar to the Voyager 2 violet filter, used by Ingersoll, *et al.* (1981) to establish the average zonal wind as a function of latitude. Table 1 lists the characteristics of the images. Although a sequence of 4 images separated in time by equal increments of 9.925 hrs. (the rotation period of Jupiter) would be ideal, the following table, containing frames selected to span a selected range of longitudes, illustrates the degree of compromise that was required to utilize allocated observing time to attain the goals of all campaign participants while providing continuing observing time for the rest of the astronomical community.

Images in Table 1 were cleaned to remove cosmic ray impacts and a least squares fit of the limb was used to determine the center of the planet. At the time of observations, the range to the planet was 764,450,000 km, subspacecraft latitude was −3.00°, subspacecraft longitude is tabulated as the CM (central meridian) in Table 1, subsolar latitude is −3.12° and subsolar longitude is 10–11 degrees less than the CM (east). Polar (R_p) and equatorial radii (R_e) were assumed to be 66,854 and 71,492 km, respectively. Large scale limb darkening was removed, using the Minnaert function with $k = 0.6$. Maps centered on the same central latitude and longitude were constructed from all four images. In an effort to select cloud features that are true markers of the local winds, software which allowed sequential display of the mapped time sequence was utilized and cloud features were selected based on their evolution in the time sequence. Because desirable wind tracers in rapidly moving cloud systems evolved rapidly, their horizontal displacement was determined in the last two frames (separated by 21 hours) and the resulting displacement vector reduced to zonal and meridional components.

Measured east-west rates of translation of selected clouds are plotted in Figure 2 as a function of planetographic latitude. Planetographic latitude is defined as the angle of intersection of a local normal with the equatorial plane of the planet. On an elliptical

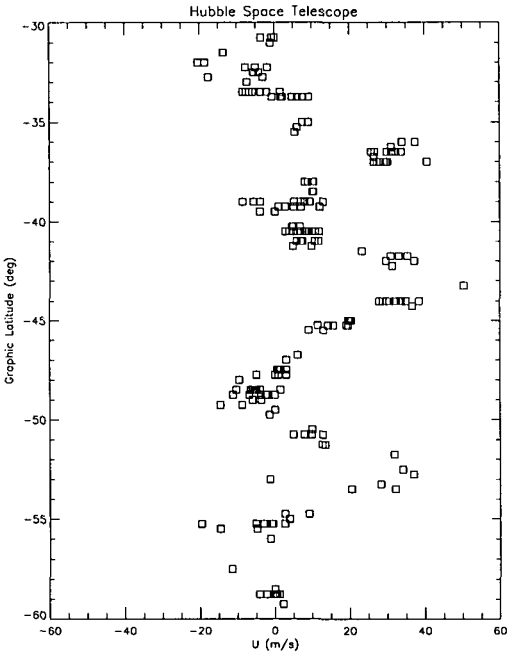

FIGURE 2. Zonal wind as a function of planetographic latitude.

planet such as Jupiter, the normal to a local equipressure surface (corresponding roughly to the cloud deck) passes through the center of the planet only at 0° and 90°. Planetocentric latitude is defined as the angle subtended between the equatorial plane and a vector passing through the planet center and a local point on the planet. Although the magnitudes of planetographic (θ_g) and planetocentric (θ_c) latitude converge at 0° and 90°, planetographic latitude is larger at all other latitudes and the relation between the two is:

$$tan(\theta_g) = (R_e/R_p)^2 tan(\theta_c) \tag{2.2}$$

and $(R_e/R_p)^2 = 1.14356$ for Jupiter.

Using a least squares fitting routine, the planet center can be located to within 0.02 degrees in longitude and latitude if sufficient limb is present in the images. Pixelation of images in PC mode is such that a displacement of 1 pixel/20 hrs corresponds to 3–4 m s^{-1}, thus the measuring error associated with individual points in Figure 2 is on the order of 8 m s^{-1}. Dispersions greater than this at a given latitude are due to the local turbulent flow.

When the resulting wind profile is compared to Voyager results (Ingersoll, *et al.* 1981), the magnitude of the winds and latitudes of minima and maxima are the same to within the measuring error for latitudes ranging from −60° to −30°. Although the White Ovals (FA, DE and BC—left to right in Figure 1) have drifted closer together than they have ever been since their formation in 1938 and the number of small anticyclonic systems at −40° (north of the impact sites in Fig. 1) is now 6 compared to 12 during the Voyager era, the zonal wind component as a function of latitude is unaltered. This implies that the zonal wind profile is not readily altered by typical tropospheric changes and that Jovian meteorology differs greatly from that on Earth. Unlike terrestrial storm systems, Jovian meteorology is dominated by the strong east-west flow. Tropospheric cloud systems which are generated in response to convective disturbances cannot migrate north or south but are trapped and driven by the strong, nearly constant, east-west wind field.

https://doi.org/10.1017/S0252921100115568 Published online by Cambridge University Press

Site	Latitude centric	Latitude graphic	Longitude† Sys. III °	Other Nearby Sites	Δ long‡ °	Δ t hrs.
B	−42.8	−46.6	71.1	Q1	−4.8	89.37
				N	2.0	79.57
D	−43.3	−47.1	33.5	G	−6.1	19.71
				S	0.5	99.45
N	−43.4	−47.3	73.1	B	−2.0	−79.57
Q2	−44.7	−48.5	47.5	R	−3.9	9.80

† Hammel, *et al.* (1995). Longitudes are determined to ±2°

‡ Δ longitude is the estimated difference in longitude from impact center to impact center and Δ t is the time elapsed between impacts of sites within 10 degrees of specified site.

TABLE 2. Impact locations and competing impact sites

3. Temporal behavior of SL9 impact sites

SL9 impact sites can be divided into classes based on the size of the site. The sizes vary from sites that are barely detectable in the PC frames (subtending 170 km/pixel at the subspacecraft point) to site L, with visible ejecta extending from −65° to −30° latitude when the site is viewed near the terminator (sunset line) 4 days after impact (see 3.3.2). Because evolution of a site will depend on conditions of the initial impact as well as interaction with the local wind field after the ejecta enter the lower stratosphere and troposphere, several examples from the small, intermediate and large sites (Hammel, *et al.* 1995) are presented to illustrate the degree of variability in the evolution of impact sites.

3.1. *Small sites*

Impact sites associated with faint fragments (Weaver, *et al.* 1995) that can be characterized with the WFPC2 data are B, D, Q2 and N. Although these features are difficult to resolve in the WF mode, their color dependence in images obtained with filters that sound down to the ammonia cloud deck is similar to that of larger sites, and, like larger sites, they tend to be bright in the 889-nm images. Whether the observed structures of these small sites have formed from ejected material or residue from the bolide that was generated when the fragment entered the atmosphere is not clear (see chapter by Hammel). The morphology and time dependence of these features are reviewed in this section.

3.1.1. *Position of impacts relative to the wind field*

All four fragments entered the atmosphere in a region of cyclonic wind shear. Table 2 summarizes the impact locations. Relative to the System III rotation rate (870.536° day^{-1}), the zonal winds (see Fig. 2) have latitudinal shears of 6.67 m s^{-1} deg^{-1} from −49.0° to −47.5°, 3.2 m s^{-1} deg^{-1} from −47.5° to −45.5°, and more than 10 m s^{-1} deg^{-1} from −45.5° to −43.0° latitude. Thus B, D and N entered the atmosphere in a region with little latitudinal shear in the zonal winds, while Q2 impacted in a region where the shear is a factor of 2 larger.

λ_{eff} nm	Frame ID	Time dd hh mm	Lat	Long	μ_0	μ	Lat	Long	μ_0	μ
			B Site				*D Site*			
225	u2fi0g07	17 15 39	−46.8	72.5	0.72	0.70	−47.6	33.5	0.61	0.67
336	u2fi0g06	17 15 33	−46.8	72.5	0.71	0.68	−47.5	34.3	0.63	0.68
410	u2fi0g05	17 15 30	−47.0	72.5	0.70	0.67	−47.4	34.1	0.64	0.69
889	u2fi0g01	17 15 19					−47.3	33.9	0.68	0.71
410	u2fi0v01	19 07 46					−47.5	34.4	0.50	0.59
			N Site				*Q Site*			
410	u2fi0c05	21 09 35	−48.1	71.5	0.68	0.70	−48.1	46.8	0.54	0.62
889	u2fi0c01	21 09 24	−47.9	71.6	0.70	0.71	−48.3	47.0	0.59	0.65

TABLE 3. July 1994 Observational parameters of visible centers small sites

3.1.2. *The reflectivity and dispersal of small sites*

From Table 2 it is apparent that site B is the only small site that is located in an undisturbed region for more than 20 hours. However, the B fragment generated the smallest impact site, which is not bright in the 889-nm filter. Figure 3 is a map of the B and D sites constructed from (top to bottom) F255W, F336W, F410M and 889-nm methane images. Although site B shows no brightening at 889 nm, a comparison of site B with surrounding dark tropospheric features in 255, 336 and 410-nm images is consistent with dark material located higher in the atmosphere than the other dark features, where it is not as affected by overlying aerosol and Rayleigh scattering. Figure 4 contains 410-nm images where the top image is the third image in Figure 3. The second image is a 410-nm image 42.3 hours later and the bottom two are 410 and 889-nm images obtained about 90 hours after those in Figure 3, when the N and Q2 fragments are present. Here both sites are visible as faint bright spots in the 889-nm image and comparison of the B and N sites indicates that B was no longer visible when N entered. (Note: color dependence implies the dark particles were at high altitudes where zonal wind velocities should be small. Evaporation or growth of particles may affect the optical depth of the debris.) Table 3 lists image ID, time of observation, latitude and longitude of the center of the observed sites, and cosine of incident and emergent angles of site centers (the optical path is inversely proportional to the cosine of the angles for the optically thin case).

The G impact occurred on July 18 at 7:35 UT, contaminating the small D site in the 2 lower frames in Figure 4. Comparison of the top 3 frames in Figure 4 indicates that site D dispersed westward, which is consistent with the sense of the underlying tropospheric winds (see Fig. 2) and indicates that some of the dark material was deposited or had migrated down to the lower stratosphere. In the two bottom frames in Figure 4 site Q2 is east and site N is west of the intermediate Q1 site. Site R is east of Q2. The N and Q2 fragments impacted on July 20 and during the following three day period of the HST/SL9 intensive observing program they changed very little. Thus, these limited observations indicate that only D, the largest of the four sites, perturbed by the nearby impact of G, has dark material extending low enough into the stratosphere to interact with the tropospheric winds during this period.

3.2. *Intermediate Sites*

Table 4 contains impact parameters for the individual intermediate sites. The fact that R and S arrived later than G and impacted less than 17 degrees west of this large site

FIGURE 3. Comparison of the B site in filters with effective wavelengths of (top to bottom) 255, 336, 410, and 889 nm.

https://doi.org/10.1017/S0252921100115568 Published online by Cambridge University Press

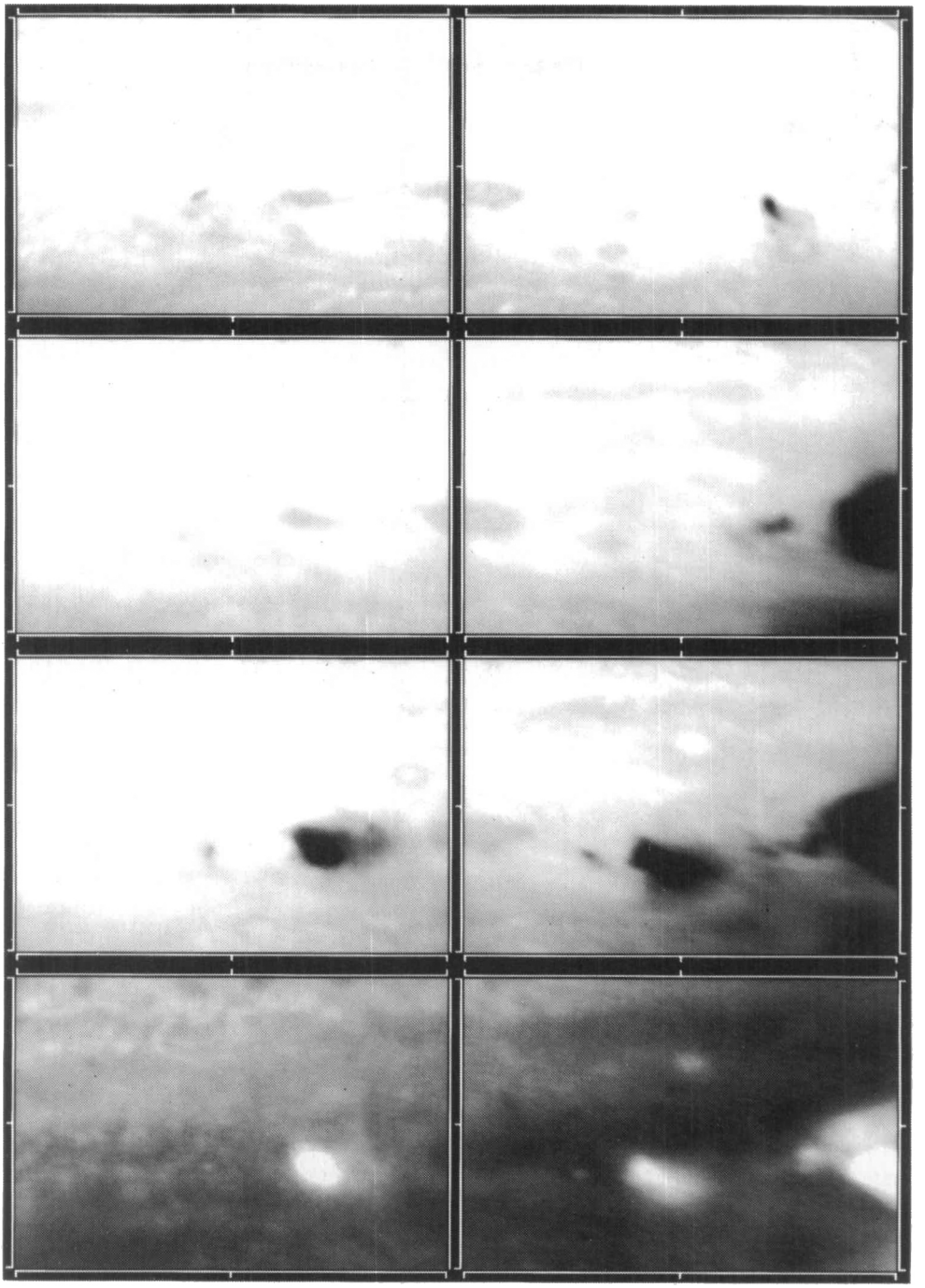

FIGURE 4. Comparison of sites B, D, N, and Q2 in filters with effective wavelengths of 410 (top three) and 889 nm (bottom).

https://doi.org/10.1017/S0252921100115568 Published online by Cambridge University Press

Site	Latitude Planetocentric	Latitude Planetographic	Longitude System III
S	−43.91	−47.75	34.0
R	−44.17	−48.00	46.8
Q1	−43.41	−47.02	66.3
H	−43.66	−47.27	101.4
E	−44.54	−48.14	152.5
A	−43.54	−47.15	186.3
C	−43.41	−47.02	225.0

TABLE 4. Impact location of uncontaminated intermediate sites

confuses the structures associated with these fragments to the point that little insight can be gained concerning the interaction of these sites with the undisturbed environment. Sites A, C, E, H, and Q1 were relatively well observed during the SL9 campaign and are reviewed below.

3.2.1. *Position in the zonal winds*

Hammel, *et al.* (1995) describe sites A, C, E, H, Q1, R, and S as intermediate in size. These fragments impacted at latitudes where zonal winds ranged from −5 to 5 m s^{-1}, however, if the ejecta from the sites were at a level where it was sensitive to the zonal wind field, an expansion greater than 2° (1750 km) to the north or south of the impact latitude would carry the debris into eastward (to the north) or westward (to the south) shear zones.

3.2.2. *Sites C, A and E*

Because some HST orbits were dedicated to UV imaging, in order to obtain the earliest combined view of sites C, A, and E (left to right), latitude-longitude maps from images obtained with the F336W filter instead of the F410M filter are presented in Figure 5. The data used to construct the upper map were obtained on July 17 at 18h 42m, 11.47, 22.48, and 3.50 hrs. after impacts A, C, and E, respectively. The lower map, from data obtained on July 23 at 14h 42m UT, illustrates the evolution of the features over a five day period. Note that site A has become entrained around the perimeter of a white cloud at −51° latitude that has the morphology of an anticyclonic system. This system is moving eastward at a rate of about 1.6° day^{-1} (16 m s^{-1}). Figure 5 illustrates the sensitivity of evolution of impact sites to local tropospheric cloud systems. Here C and E dispersed in a manner that is consistent with the mean tropospheric zonal winds, but site A is drastically modified by the presence of a well-developed anticyclonic storm system.

3.2.3. *Site H*

Evolution of the H site has been modified by the presence of an anticyclonic system to the north of the feature at −40° latitude, drifting eastward at a rate of 0.4° day^{-1} (4 m s^{-1}) relative to System III. Figure 6 contains a sequence of map projections that reveals the development of the site during its first 5 days. Corresponding information on times of observation is tabulated in Table 5.

Maps in Figure 6 are centered on −48° latitude and 99.5° longitude and extend ±15° in both latitude and longitude. The average zonal wind field has been utilized to compute the actual longitudinal translation of the cloud deck that would occur between the times

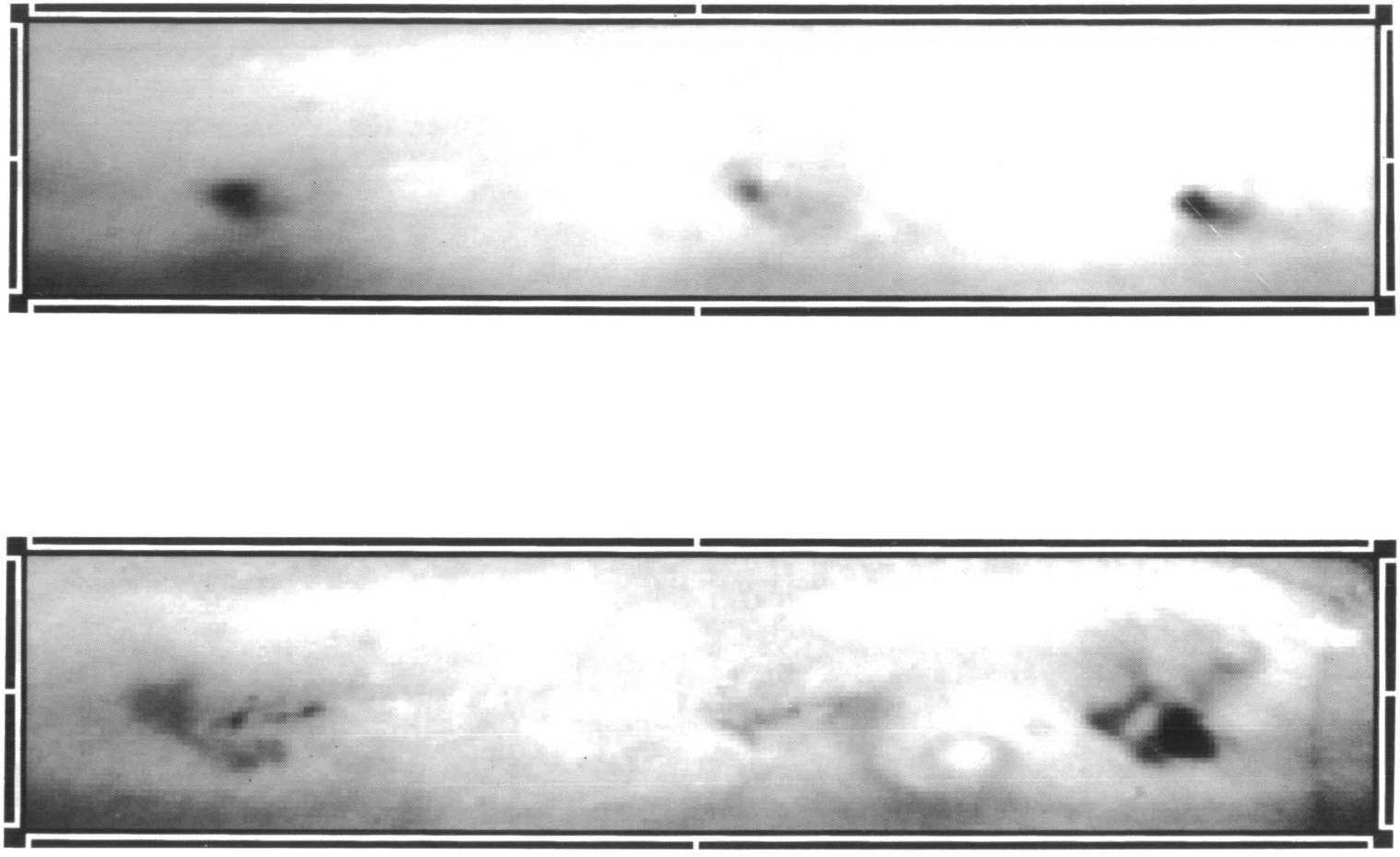

FIGURE 5. Evolution of intermediate sites C, A, and E. The two maps were generated from images obtained on July 17, when all sites were less than 24 hrs. old, and from a second image 5 days later.

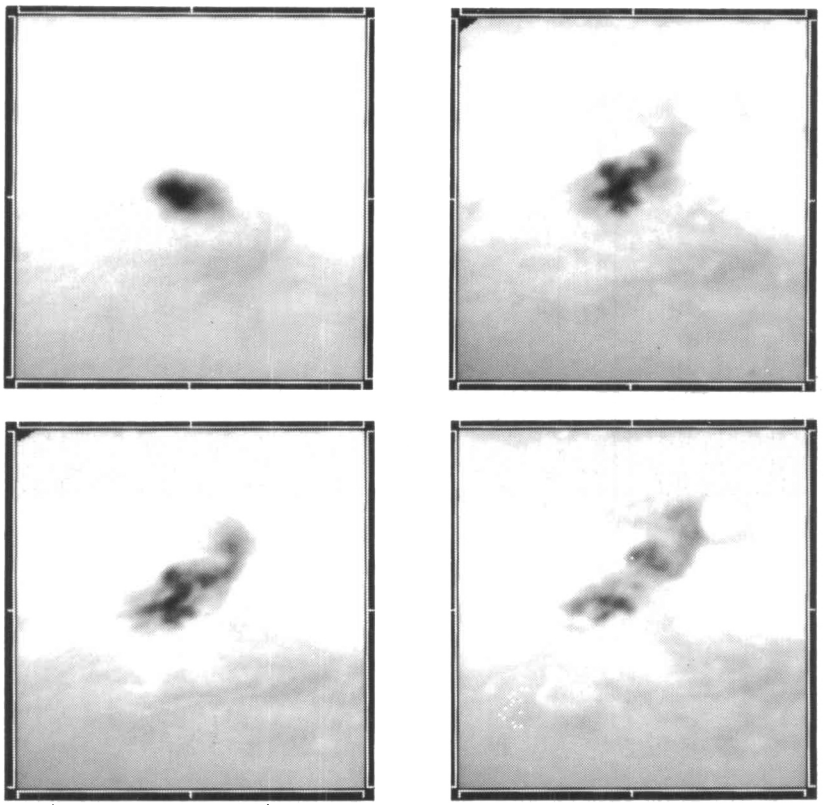

FIGURE 6. Evolution of site H. The maps at upper left, upper right, lower left and lower right are 12.2, 62.0, 81.5, and 111.9 hours after impact of the fragment, respectively. The dotted line superimposed on the lower right map represents tropospheric cloud displacement over 52 hrs., the difference in time between the upper right and lower right figures.

ID	Time dd hh mm	Δ t since impact hrs
u2fi0v05	19 07 46	12.2
u2fi1c05	21 09 35	62.0
u2fi1l05	22 04 53	81.5
u2fi1u05	23 11 26	111.9

TABLE 5. Observational parameters of Site H images

of acquisition of u2fi1c05 (upper right) and u2fi1u05 (lower right). The winds range from −10 to 15 m s^{-1} in this region and during the intervening 50 hours the underlying clouds translated as much as 10° in longitude. In general, average meridional motion of Jovian clouds is not detectable at this spatial resolution unless a closed turbulent cyclonic system is present. In this case, though, a northward velocity of 25 m s^{-1} is required to attain the observed expansion. This figure illustrates that the dark ejecta become entrained in lower stratospheric winds and, although some entrainment occurred around the bright anticyclonic feature, some of the dark material continued northward where it was swept into the westward flow around the northward edge of the storm center.

https://doi.org/10.1017/S0252921100115568 Published online by Cambridge University Press

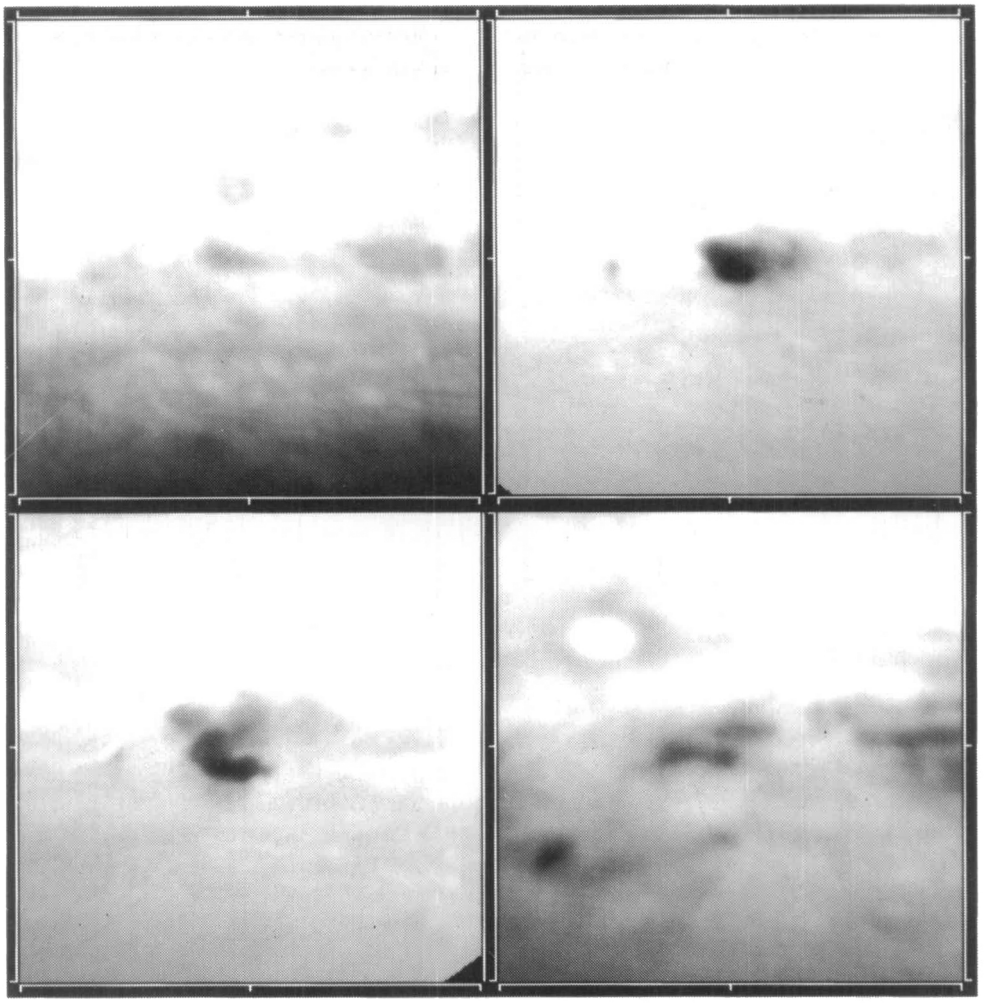

FIGURE 7. Development of the Q1 site over more than a month.

3.2.4. *Site Q1*

Figure 7 shows the longterm development of site Q1, an intermediate with no nearby anticyclonic systems at the time of impact. These maps are centered on $-47.5°$ latitude and 64° longitude. They extend $\pm 15°$ in both latitude and longitude. During the pre-impact phase two dark spots at the latitude of the impact extended from 57.1° to 51.4° (eastern spot) and 67.3° to 63.25° (western spot). During the week that the SL9 impacts occurred, these features changed very little, indicating minimum turbulence associated with typical tropospheric low albedo regions at this latitude. The time sequence (upper left, upper right, and lower left) reveals a small white oval surrounded by a dark collar which was translating eastward at a rate of 3.5° day^{-1} (34 m s^{-1}). Passage of this feature perturbed the structure of the Q1 ejecta. On August 23 a white oval was located northwest of site Q1 (lower right). This anticyclonic structure was centered at $-40.5°$ latitude and 72.3° longitude. It was translating eastward at a rate of 0.61° day^{-1} (6.8 m s^{-1}). This was the same white oval that was interacting with site H on July 23. During the first week site Q1 was not greatly perturbed by local storm systems. By August 23, it

https://doi.org/10.1017/S0252921100115568 Published online by Cambridge University Press

ID	Time m dd hh mm	Δ t since impact hrs
u2fi0v05	07 19 07 46	−60.6
u2fi1c05	07 21 09 35	13.4
u2fi1t05	02 23 09 49	61.5
u2fi2n05	08 23 02 54	798.8 (33.3 days)

TABLE 6. Observational parameters of Site Q1 images

Site	Latitude Planetocentric	Latitude Planetographic	Longitude System III	Time of Impact dd hh mm
G	−43.66	−47.27	26.8	18 07 35
K	−43.29	−46.90	282.6	19 10 31
L	−42.79	−46.40	351.6	19 22 21

TABLE 7. Impact location of large sites

was extending to the west of the impact sight in agreement with reduced stratospheric winds that reflect the mean zonal flow of the troposphere.

3.3. *Large sites*

3.3.1. *Position in the zonal winds*

Based on the brightness of pre-impact fragments, Weaver, *et al.* (1995) rated sites G, K, and L as class 1 or large sites. Unfortunately, sites K and G were not temporally well sampled; however, comparisons can be made among the three. Table 7 contains parameters related to the large impacts. Although these fragments entered the atmosphere at a latitude where the mean zonal winds are small, they were bounded on the south by a tropospheric jet with maximum westward winds of 10–15 m s^{-1} centered near 48.5° latitude. Because the ejecta have been thrown high into the atmosphere above aerosol and Rayleigh scatterers (Munoz, *et al.* 1996), obscuration due to comet ejecta will be particularly sensitive to effective path length through the absorbers and most visible near the planet limb (note: this is markedly different from Jovian tropospheric features, which are dark at wavelengths between 0.5 and 1 micron. They brighten near the limb or terminator where high altitude scattering greatly reduces contrast with surrounding clouds). The top right and left images in Figure 8 show site L rotating onto the western limb of the planet and approaching the eastern terminator, respectively. The lower images are of site K (left) crossing the limb and site G (right) approaching the limb. It is apparent that material ejected from site L spans latitudes from −65° to −30°. Material that is ejected further south than −50° or that extending northward would be entrained in an eastward flow on return to the lower stratosphere or troposphere. Comparison of sites K and L indicates that K ejecta were not as wide spread as those from the site L and, although the R and S impacts have entered near site G, the total latitudinal dispersion is not greater than that from site L.

3.3.2. *Site L*

Figure 9 shows three stages of development of site L. The site was observed 22.6 (left), 32.1 (center), and 81.9 (right) hours after impact. The dotted profile on the right map shows translational motion of tropospheric features drifting with the mean zonal

https://doi.org/10.1017/S0252921100115568 Published online by Cambridge University Press

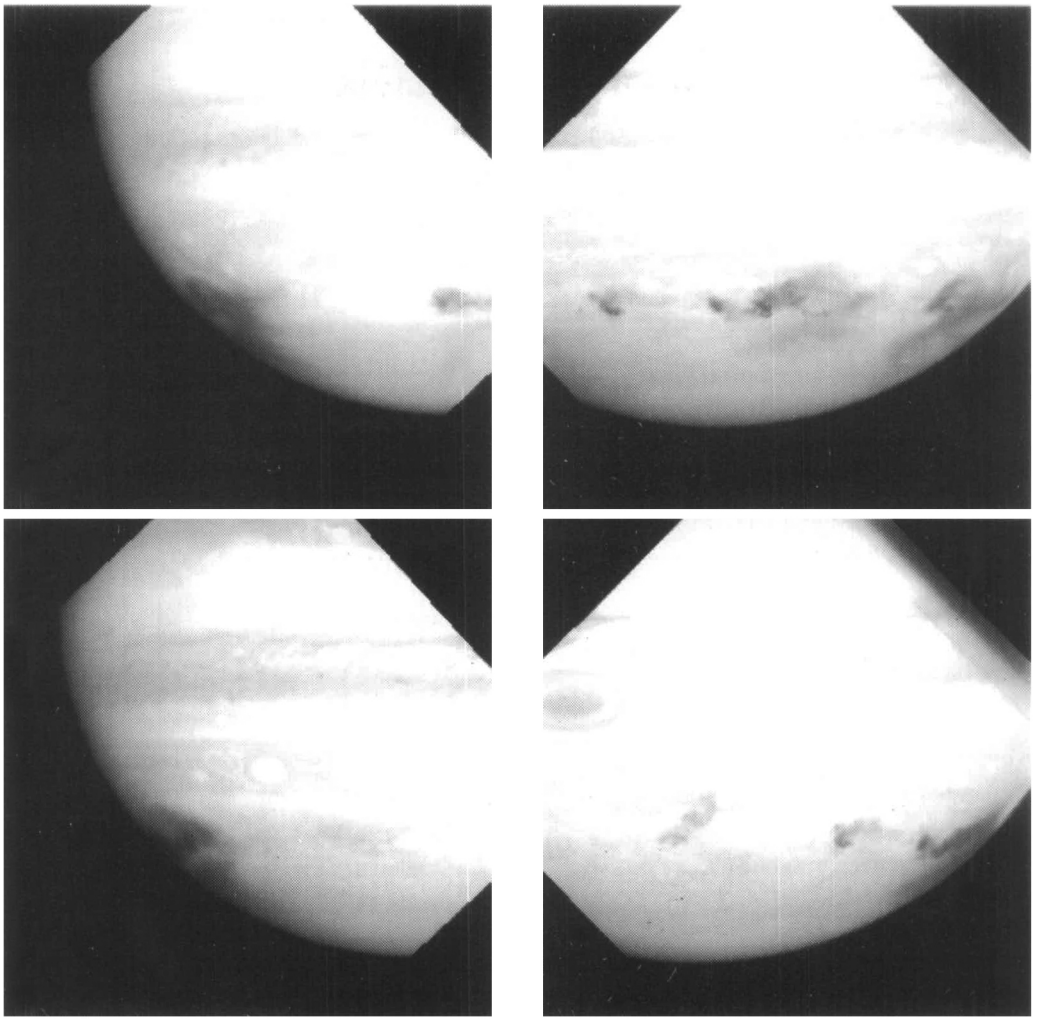

FIGURE 8. Terminator and limb views of sites G, L and K.

winds that would occur during 49.8 hours that have elapsed between the center and right images. Comparison of the three images suggests rotation about the impact center. The measured translation of dark structures around the westernmost perimeter of the darkest region implies an anticyclonic rotation with perimeter velocities on the order of 45 m s^{-1}. At the same time, a dark region to the southeast of the impact center expands eastward 1.2° of longitude over this 82-hour interval.

Table 8 contains the observational parameters for site L. Comparison of these parameters with those in Table 5 reveals that both sites H and L were observed about 81 hours after impact. Figure 10 is a comparison of site L (upper) and site H (lower). The left images show the impact sites before arrival of the L and H fragments, the central (410-nm) and right (889-nm) images compare the sites 81.5 hours after impact. Note that in the case of site L, the dark streak was not disturbed by impact L. There is a well-formed cyclonic storm center to the north of the site and the dark material does not encroach into it. Simon & Beebe (1996) measured winds of about 45 m s^{-1} around the northern perimeter of this system. The return westward flow along its southern edge was less

https://doi.org/10.1017/S0252921100115568 Published online by Cambridge University Press

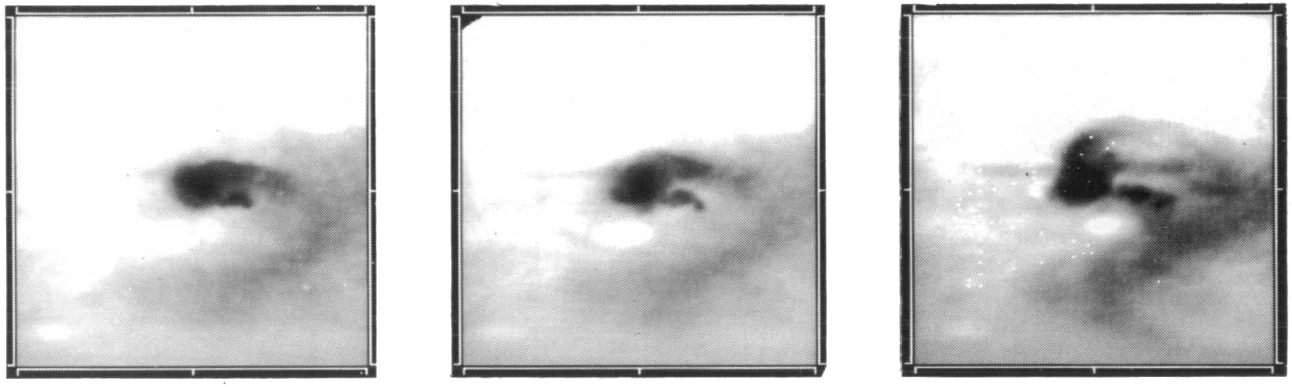

FIGURE 9. Evolution of site L. These 3 images, obtained with the 410-nm filter show the evolution of the site during its first 82 hours.

ID	Time dd hh mm	Δ t since impact hrs
u2fi6803	20 20 56	22.6
u2fi1905	21 06 28	32.1
u2fi1s05	23 08 12	81.9

TABLE 8. Observational parameters of Site L images

organized but of similar magnitude. Such a system should have a central subsidence, and conservation of mass flow would require upwelling around the perimeter. Observed morphology of site L suggests that this local upwelling constrains northward expansion of the ejecta. Because the local flow is westward, this local storm cell could contribute to the counterclockwise rotation of more southerly dark material.

A bright oval centered at −51° latitude drifts eastward at a rate of about 1.6° day^{-1} (16 m s^{-1}). During the time since impact it has shifted eastward 5.5° relative to the impact site. The central upwelling associated with this anticyclonic system would be associated with subsidence around the perimeter of the cloud system. This would encourage concentration of dark particles along the southern perimeter of the impact site near −49° latitude.

The fact that the underlying dark tropospheric streak (Figure 10—upper left) appears undisturbed limits the extent to which the L impact has disturbed the local troposphere and is consistent with either shallow penetration of the impactor or a clean entry and exit of a more deeply penetrating fragment. Failure of the dark material to disperse according to the predicted pattern inferred by the mean tropospheric zonal flow, along with the constrained nature of the core of the impact site and apparent rotational speed, are consistent with a rising central region. However, the fact that the expanding stratospheric material encounters a westward flow to the north and a well-formed anticyclonic system is passing to the south can impose the observed structure on the expanding ejecta. Comparison of the 410 and 889-nm images of site H in Figure 10 (lower central and right images, respectively) with those of site L (upper center and right images) when both sites were about 82 hours old does not infer stronger upwelling at site L. In addition, visibility of anticyclonic storm centers in the 889-nm images (upper and lower right) in Figure 10 demonstrates that these systems are elevated and their associated circulation could influence dispersion of the dark ejecta.

The manner in which intermediate sites A and H responded to nearby anticyclonic systems is consistent with this interpretation of the evolution of site L. Inspection of the H impact site in Figure 10 (lower left) reveals that the fragment entered a local turbulent cyclonic system. The flocculent structure of site H in Figure 6 is consistent with local entrainment into the vertical motions within the system.

3.3.3. *Sites G and K*

The well-known "Bull's eye" was imaged on July 18, 1.5 hr. after impact (Ingersoll & Kanamori, 1996). Due to the fact that fragments R and S entered the atmosphere near site G, evolution of the original site is confusing but comparison with the ejecta blanket from sites L and K in Figure 8 indicates that ejecta from the G complex were more extensive than that from K.

From the time of impact of the K fragment until July 23, when a set of images containing sites L, K and G was obtained, no clear view of site K was acquired with the WFPC2.

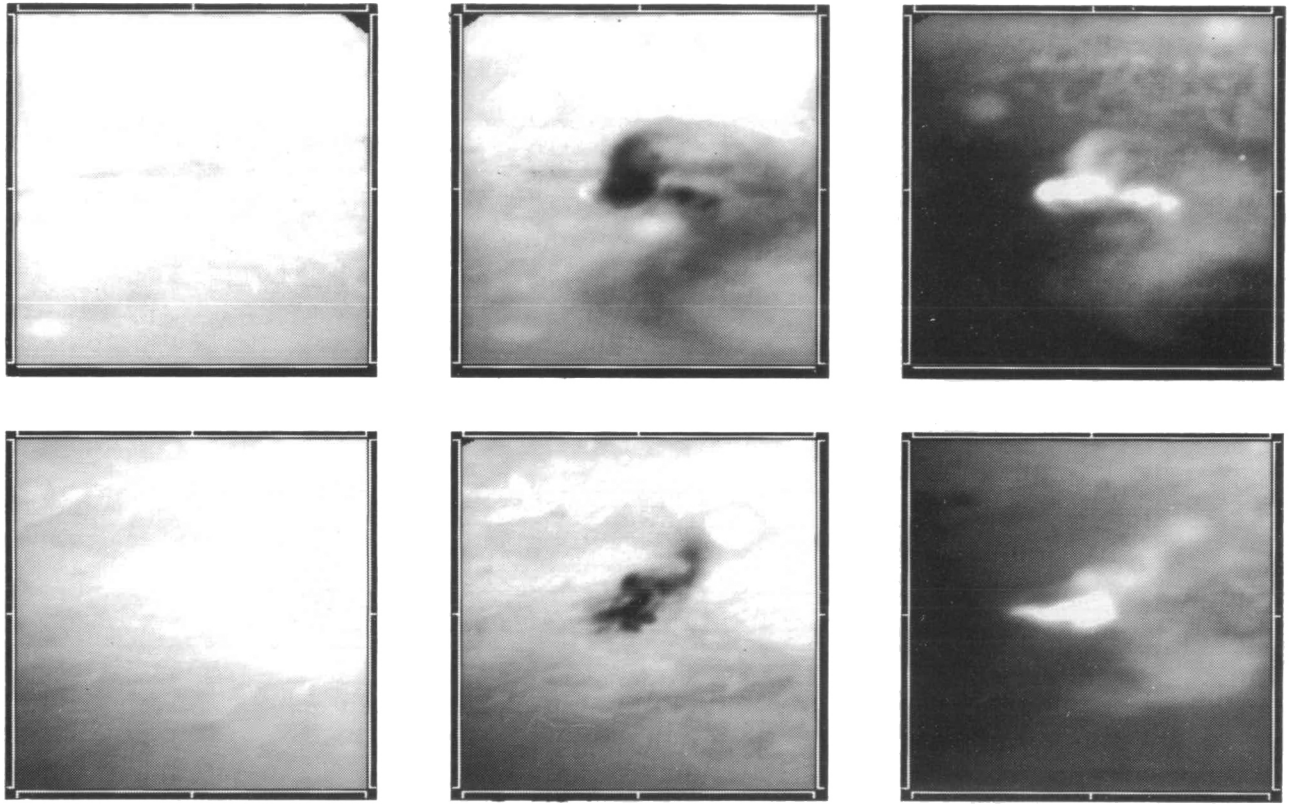

FIGURE 10. *Comparison of local cloud structure and vertical development of sites L and H. The left maps show the sites before impact and the center and right maps are from 410-nm and 889-nm images about 82 hours after impact.*

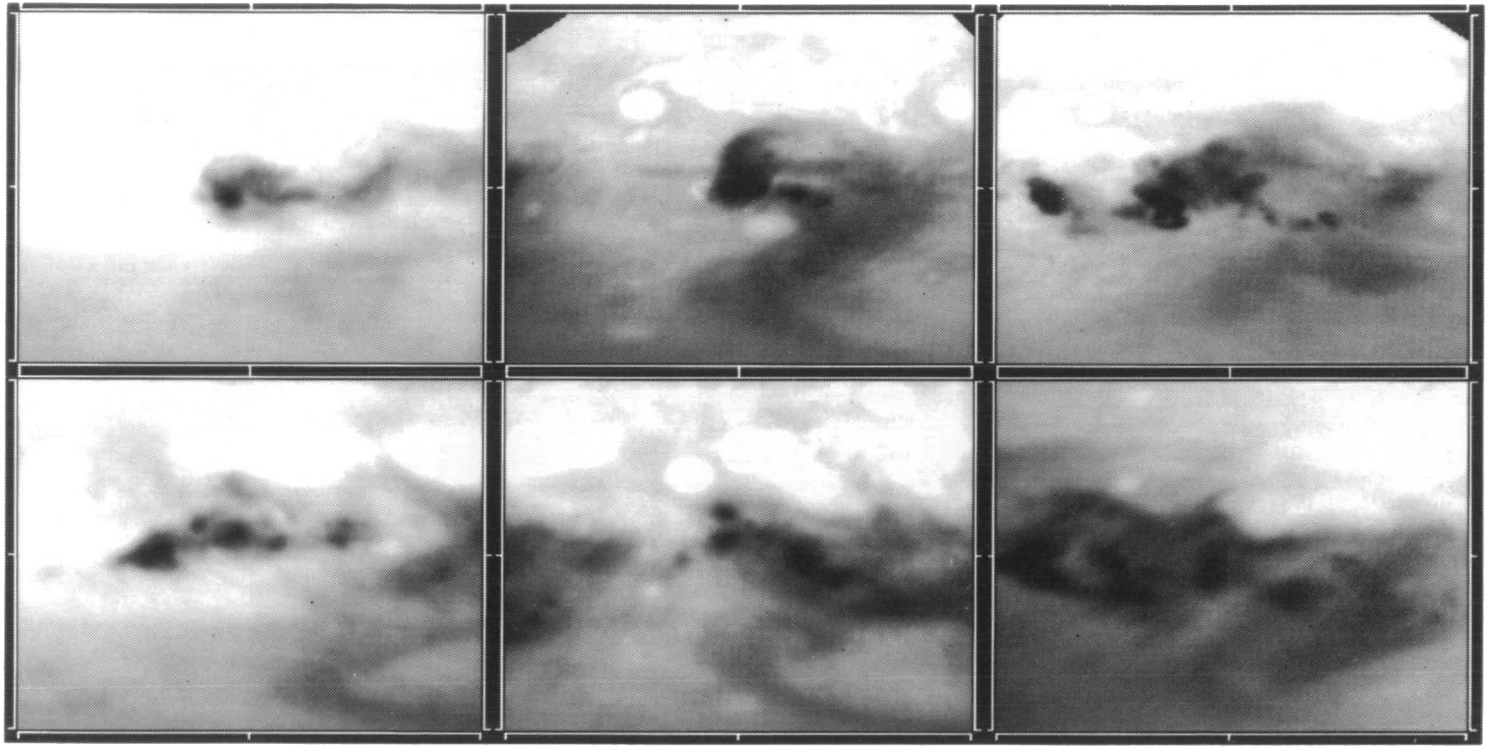

FIGURE 11. Dispersion of sites K, L and G. K is on the left, L is at center and G is on the right.

By the time of acquisition of the July 23 image more than 92 hours had elapsed since the K impact occurred. A comparison of a limb view of K with that of L (See Figure 8) indicates that K had a less extended ejecta blanket. Simon & Beebe (1996) have shown that, during the first 92 hours, site K evolved in a manner that indicated that it was not strongly influenced by local weather systems. It was dispersing as predicted by the mean zonal flow.

Figure 11 compares the evolution of sites K (left) and G (right) sites with site L (center) during the week following the final impacts. The top maps were obtained on July 23 and the lower on July 30. These maps are centered at $-47.5°$ latitude and at the impact longitudes, 283° (left—site K) 352° (center—site L) and 27° (right—site G). The maps extend $\pm 15°$ in latitude and $\pm 20°$ in longitude.

During this period the dispersal of the dark material is consistent with subsidence into the region where the mean zonal winds dominate the circulation. Similarity of the dispersal of passive site K and site L is further evidence that the anticyclonic morphology of site L was not internally driven.

4. Conclusions

SL9 WFPC2 data provide a high resolution wind profile, which can be compared with that derived from the Voyager imaging data. Although the wind profile indicates no significant differences in magnitude or location of the wind maxima and wind minima, the longitudinal spacing associated with cyclonic-anticyclonic weather systems at $-41°$ latitude is a factor of 2 larger for the SL9 era. This result has significant implications. It supports the argument that the winds are deep-seated, driven by an internal heat source and that the meteorology is constrained by the prevailing winds. Morphology differences may be generated by variations in vertical transport rates within this stable zonal flow.

Morphology of small sites indicates that dark material is present even for site B, which is not detectable as a bright patch in the 889-nm image. This can imply that the dark material formed during the bolide stage as well as later.

Evolution of individual impact sites is complex and varies from site to site. Initial ejecta blankets extend from $-65°$ to $-30°$ latitude and contain considerable radial structure relative to the impact site. Although the sites are modified by nearby impacts, they are much more influenced by local cyclonic and anticyclonic storm systems. Gierasch, Conrath & Magalhaes (1986) have shown that the zonal winds decrease with altitude within 2 to 3 scale heights (50–75 km). Although this decrease in the zonal winds is expected due to frictional drag in the atmosphere, evolution of SL9 impact sites infers that circulation associated with well-formed cyclonic and anticyclonic storm centers does not decrease as rapidly with height and has considerable influence on developing morphology of the impact site. This indicates that circulation within the lower stratosphere would deviate from the mean flow above both well-formed cyclonic and anticyclonic storms.

The complexity and latitudinal extent of the initial ejecta blanket and the extent of dispersal of the impact sites depend on the local tropospheric weather systems. Cyclonic systems, with upwelling around the perimeter, tend to constrain and inhibit northward expansion. In comparison, downwelling around the perimeter of anticyclonic systems to the north and south of the sites entrains the dark ejecta.

REFERENCES

BEEBE, R. F. & YOUNGBLOOD, L. A. 1979 Pre-Voyager velocities, accelerations and shrinkage rates of Jovian cloud features. *Nature* **280**, 771–772.

BEEBE, R. F., ORTON G. S. & WEST R. A. 1989 Time-variable nature of the Jovian cloud properties and thermal structure: an observational perspective. In *Time-Variable Phenomena in the Jovian System* (ed. M. J. S. Belton, R. A. West and J. Rahe). NASA SP-494, 245–288.

BURROWS, C. J., CLAMPIN, M., GRIFFITHS, R. E., KRIST, J., & MACKENTY, J. W. 1994 WFPC2 instrument handbook, version 2.0. Space Telescope Science Institute.

CHAPMAN, C. R. 1969 Jupiter's zonal winds: variation with latitude. *J. Atmos. Sci.* **26**, 986–990.

DOWLING, T. E. & INGERSOLL, A. P. 1989 Jupiter's Great Red Spot as a shallow water system. *J. Atmos. Sci.* **46**, 3256–78.

DOWLING, T. E. 1993 A relationship between potential vorticity and zonal wind on Jupiter. *Science* **50**, 14–22.

GIERASCH, P. J., CONRATH, B. J., & MAGALHAES, J. A. 1986 Zonal mean properties of Jupiter's upper troposphere from Voyager infrared observations. *Icarus* **67**, 456–483.

GIERASCH, P. J. & CONRATH, B. J. 1993 Dynamics of the atmosphere of the outer planets: post-Voyager measurement objectives. *J. Geophys. Res.* **98**, 5459–5469.

HAMMEL,H. B., BEEBE, R. F., INGERSOLL, A. P., ORTON. G. S., MILLS, J. R., SIMON, A. A., CHODAS, P., CLARKE, J. T., DE JONG, E., DOWLING, T. E., HARRINGTON, J., HUBER, L. E., KARKOSCHKA, E., SANTORI, C. M., TOIGO, A., YEOMANS, D. & WEST, R. A. 1995 Hubble Space Telescope imaging of Jupiter: atmospheric phenomenon created by the impact of comet Shoemaker-Levy 9. *Science* **267**, 1288–1296.

HOLTZMAN, J., HESTER, J. J., CASERTANO, S., TRAUGER, J. T., WATSON, A. M., BALLESTER, G. E., BURROWS, C. J., CLARKE, J. T., CRISP, D., EVANS, R. W., GALLAGHER III, J. S., GRIFFITHS, R. E., HOSSEL, J. G., MATTHEWS, L. D., MOULD, R. J., SCOWEN, P. A., STAPELFELDT, K. R., & WESTPHAL, J. A. 1995 The performance and calibration of WFPC2 on the Hubble Space Telescope. *PASP* **107**, 156–178.

INGERSOLL, A. P. & CUZZI, J. N. 1969 Dynamics of Jupiter's cloud bands. *J. Atmos. Sci.* **26**, 981–985.

INGERSOLL, A. P. BEEBE, R. F., MITCHELL, J. L., GARNEAU, G. W., YAGI, G. M., & MULLER, J. P. 1981 Interactions of eddies and mean zonal flow on Jupiter as inferred from Voyager 1 and 2 images. *J. Geophys. Res.* **86**, 8733–8743.

INGERSOLL, A. P., BEEBE, R. F., CONRATH, B. J. & HUNT, G. E. 1984 Structure and dynamics of Saturn's atmosphere. In *Saturn* (ed. T. Gehrels & M. S. Matthews), pp. 195–238. Arizona Press.

INGERSOLL, A. P. AND KANAMORI, H. 1996 Two waves from SL9 to probe the Jovian water cloud. *Icarus* Special SL-9 Issue (in press).

LIMAYE, S. S., REVERCOMB, H. E., SROMOVSKY, L. A., KRAUSS, R. J., SANTEK, D. A., SUOMI, V. E., COLLINS, S. A., & AVIS, C. C. 1982 Jovian winds from Voyager 2, part I: zonal mean circulation. *J. Atmos. Sci.* **39**, 1413–1432.

LIMAYE, S. S. 1986 Jupiter: new estimates of the mean zonal flow at the cloud level. *Icarus* **65**, 335–352.

MARCUS, P. S. 1993 Jupiter's Great Red Spot and other vortices. *Ann. Rev. Astron. Astrophys.* **31**, 523–73.

MINNAERT, M. 1941 The reciprocity principle in lunar photometry. *Astrophys. J.* **93**, 403–410.

MUNOZ, O., MORENO, F. AND MOLINA, A. 1996 Aerosol properties of debris from fragments E/F of comet Shoemaker-Levy 9 *Icarus* Special SL9 Issue (in press).

ORTON, G. S., FRIEDSON, A. J., YANAMANDRA-FISHER, P. A., CALDWELL, J., HAMMEL, H., BAINES, K. H., BERGSTRALH, J. T., MARTIN, T. Z., WEST, R. A., VEEDER JR., G. J., LYNCH, D. K., RUSSELL, R., MALCOM, M. E., GOLISCH, W. F., GRIEP, D. M., KAMINSKI, C. D., TOKUNAGA, A. T., BARON, R., HERBST, T. & SHURE, M. 1994 Thermal maps of Jupiter: Spatial organization and time dependence of tropospheric temperatures, 1980–1993. *Science* **265**, 625–631.

PEEK, B. M. 1958 *The Planet Jupiter*. Faber and Faber.

REESE, E. R. (Private communication with longterm BAA & ALPO observer)

SIMON, A. A. AND BEEBE, R. F. 1996 Jovian tropospheric features—wind field, morphology and motion of long-lived systems. *Icarus* Special SL-9 Issue (in press).

SMITH, B. A. & HUNT, G. E. 1976 Motions and morphology of clouds in the atmosphere of Jupiter. In *Jupiter, The Giant Planet* (ed. T. Gehrels) pp. 564–585. Arizona Press.

SMITH, B. A., SODERBLOM, L. A., JOHNSON, T. V., INGERSOLL, A. P., COLLINS, S. A., SHOEMAKER, E. M., HUNT, G. E., MASURSKY, H., CARR, M., DAVIES, M. E., COOK, A. F., BOYCE, J. M., DANIELSON, G. E., OWEN, T., SAGAN, C., BEEBE, R. F., VEVERKA, J., STROM, R. G., MCCAULEY, J. F., MORRISON, D., BRIGGS, G. A. & SUOMI, V.E. 1979a The Jupiter system through the eyes of Voyager 1. *Science* **204**, 951–972.

SMITH, B. A., SODERBLOM, L. A., BEEBE, R. F., BOYCE, J. M., BRIGGS, G. A., CARR, M., COLLINS, S. A., COOK, A. F., DANIELSON, G. E., DAVIES, M. E., HUNT, G. E., INGERSOLL, A. P, JOHNSON, T. V., MASURSKY, H., MCCAULEY, J. F., MORRISON, D., OWEN, T., SAGAN, C., SHOEMAKER, E. M., STROM, R., SUOMI, V. E. & VEVERKA, J. 1979b The Galilean satellites and Jupiter: Voyager 2 imaging science results. *Science* **206**, 927–950.

WEAVER, H. A., A'HEARN, M. F., ARPIGNY, C., BOICE, D. C., FELDMAN, P. D., LARSON, S. M., LAMY, P., LEVY, D. H., MARSDEN, B. G., MEECH, K. J., NOLL, K. S., SCOTTI, J. V., SEKANINA, Z., SHOEMAKER, C. S., SHOEMAKER, E. M., SMITH, T. E., STERN, S. A., STORRS, A. D., TRAUGER, J. T., YEOMANS, D. K., & ZELLNER, B. 1995 The Hubble Space Telescope (HST) observing campaign on Comet Shoemaker-Levy 9. *Science* **267**, 1282–1287.

WEST, R. A., FRIEDSON, A. J. & APPLEBY, J. F. 1992 Jovian large-scale stratospheric circulation. *Icarus* **100**, 245–259.

WEST, R. A., STROBEL, D. F. & TOMASKO, M. G. 1986 Clouds, aerosols and photochemistry in the Jovian atmosphere. *Icarus* **65**, 161–217.

WILLIAMS, G. P. & WILSON, R. J. 1988 The stability and genesis of Rossby vortices. *J. Atmos. Sci.* **45**, 207–241.